Petroleum Science 21 (2024) 4248–4261

Contents lists available at ScienceDirect

Petroleum Science

journal homepage: www.keaipublishing.com/en/journals/petroleum-science

Original Paper

Three-dimensional fracture space characterization and conductivity evolution analysis of induced un-propped fractures in shale gas reservoirs

Bin Yang [a], Wen-Jing Ma [a, *], Guan-Chang Pan [a, b], Ke-Liu Wu [c], Ying Zhong [a], Zhang-Xin Chen [d, e]

[a] State Key Laboratory of Oil and Gas Reservoir Geology and Exploitation, Chengdu University of Technology, Chengdu, 610059, Sichuan, China
[b] Sinopec Maoming Petrochemical Company, Maoming, 525000, Guangdong, China
[c] State Key Laboratory of Petroleum Resources and Engineering, China University of Petroleum (Beijing), Beijing, 102249, China
[d] Eastern Institute of Technology, Ningbo, 31500, Zhejiang, China
[e] Department of Chemical and Petroleum Engineering, University of Calgary, Calgary, Alberta, T2N 1N4, Canada

ARTICLE INFO

Article history:
Received 3 February 2024
Received in revised form
23 July 2024
Accepted 23 July 2024
Available online 25 July 2024

Edited by Yan-Hua Sun

Keywords:
Gas shale
Induced unpropped fractures
Surface asperity
Fracture space
Stress sensitivity

ABSTRACT

Huge numbers of induced unpropped (IU) fractures are generated near propped fractures during hydraulic fracturing in shale gas reservoirs. But it is still unclear how their fracture space and conductivity evolve under in-situ conditions. This paper prepares three types of samples, namely, manually split vertical/parallel to beddings (MSV, MSP) and parallel natural fractures (NFP), to represent the varied IU fractures as well as their surface morphology. Laser scan and reconstruction demonstrate that the initial fracture spaces of MSVs and MSPs are limited as the asperities of newly created surfaces are well-matched, and the NFPs have bigger space due to inhomogeneous geological corrosion. Surface slippage and consequent asperity mismatch increase the fracture width by several times, and the increase is proportional to surface roughness. Under stressful conditions, the slipped MSVs retain the smallest residual space and conductivity due to the newly sharp asperities. Controlled by the bedding structures and clay mineral hydrations, the conductivity of MSPs decreases most after treated with a fracturing fluid. The NFPs remain the highest conductivity, benefitting from their dispersive, gentle, and strong asperities. The results reveal the diverse evolution trends of IU fractures and can provide reliable parameters for fracturing design, post-fracturing evaluation, and productivity forecasting.

1. Introduction

Successful commercial development of shale gas from extremely tight source rocks is almost entirely dependent on large-scale hydraulic fracturing of long-section horizontal wells, during which complex fracture networks are generated and the gas transport efficiency from matrix pores to boreholes is radically promoted to engineering acceptable levels. The fracture networks are multiscale systems, generally including the primary propped fractures, secondary propped and unpropped fractures. The propped fractures are high conductivity paths near a wellbore zone, and around these main fractures exist huge numbers of induced unpropped (IU) fractures. Sharma and Manchanda (2015) gave the IU fractures a broad engineering definition as fractures that have widths that are too small to accommodate any proppants and as such will close over time as the fluid pressure within them is decreased. The conductivity of IU fractures is significantly lower than that of propped fractures, but they contribute the majority part of a fractured surface area (Cipolla et al., 2010; Pathak et al., 2014) and have equal importance for the overall fracturing performance and long-term production.

The induced stresses derived from a process of creation of the main hydraulic fractures play a key role in the creation of IU fractures. These stresses can result in slippage along weakness planes such as bedding planes and other boundaries between lithologically distinct layers, the sliding of pre-existing natural faults or

* Corresponding author.
E-mail address: 1847070601@qq.com (W.-J. Ma).

https://doi.org/10.1016/j.petsci.2024.07.022

fissures, and the tensile/shear rupture of partly/highly mineralized or closed natural fractures (Roussel and Sharma, 2011). Benefitting from the generation mechanism of IU fractures, these newly created fracture surfaces cannot match well due to the combined effects of surface roughness and fracture displacement, and this provides effective fracture width and conductivity in the absence of proppants. Fredd et al. (2001) demonstrated that fractures with no surface displacement (aligned fractures) had very low conductivity, but the value of displaced fractures could rise as least two orders of magnitude. Under asperity-dominated conditions, the conductivity of IU fractures is significantly affected by a size distribution, mechanical properties and mineral compositions of asperities, the slipping distance of fracture planes and in-situ stress fields (Zhao et al., 2012; Zou et al., 2013; Zhang et al., 2014; Gensterblum et al., 2015).

The existence of surface asperities and their ability to withstand high closure stresses are the prerequisites for creating sufficient conductivity for IU fractures. According to the laser detection results of Sakaguchi et al. (2006), the heights of surface asperities of granite are intensively distributed in 1–2 mm, and Lu et al. (2022) measured close values of 0.74–1.43 mm for the Longmaxi shale with a similar method under stress-free conditions. Along with increasing closure stress, the fracture width generally decreases. A series of physical and numerical simulation results showed that high-stress loads may lead to a loss of 70%–85% of the IU fracture width, and the degree of stress sensitivity has a negative correlation with rock compressive strength, elastic modulus and fracture stiffness (Warpinski et al., 1997; Dam et al., 2000; Lu et al., 2020). Testing a series of sandstones with different elastic modulus, Wang (2016) concluded that under low closure stress conditions the sample conductivities kept a stable or slight decrease, whereas if the stress exceeds a critical value, such as the yield strength of surface asperities, the conductivities decline sharply. With similar laboratory and simulation methods, the Longmaxi shale shows diverse results at an early low stress stage, the IU fractures of shale specimens occur a large amount of deformation, and when the closure stress is more than 30 MPa, the deformation becomes relatively small (Xu, 2017; Lu et al., 2022).

In order to accurately describe the processes of fracture closure and conductivity degradation, continually updated laboratory and numerical methods are adopted to rebuild rough fracture surfaces and illustrate the mechanism of surface asperity deformation and breakage. Greenwood and Tripp (1967) firstly assumed a rough fracture surface as a plane composed of arranged balls with the same diameter, and in the following modified models the uniform balls were changed into curved surfaces, balls with different diameters (Whitehouse and Archard, 1970), and elastic spheroid (Bush et al., 1975). A fractal geometry method (Hanaor et al., 2015) was also used to depict the features of rough fractures and then guide the reconstruction of their surfaces according to parameters such as a fractal dimension and a joint roughness coefficient (JRC). However, due to the inherent complexity of IU fractures, the numerical fractures built with the above indirect method cannot fully represent the features of surface asperities. Now, the high-precision 3D laser scan and subsequent reconstruction based on scanning data make it possible to build a nearly real fracture surface (Lu et al., 2020). Meanwhile, this high-quality physical model helps engineers to better simulate the contact, stress concentration and elastic-plastic deformation of varied asperities (Wang, 2016; Kamali and Pournik, 2016; Lu et al., 2022) and obtain more reliable outcomes about the change tendency of fracture space and conductivity.

Surface slippage is another critical factor affecting the conductivity of IU fractures. Zhao et al. (2012) showed that the natural fracture conductivity of the Longmaxi shale increased along with the growth of slipping distance. When the surface dislocation exceeded 8 mm, the conductivity became stable. Meanwhile, other literature (Guo et al., 2013; Xu, 2017) also reported that compared with the initial conductivity of aligned fractures, surface sliding can promote the conductivity of the Longmaxi shale, but there was no rigorous positive correlation between conductivity and sliding distance. For the Haynesville shale in North America, Reece et al. (2014) found that after a displacement of 2–4 mm, a sample permeability decreased by about 1.5–2.5 orders of magnitude at an effective stress of 12.9 MPa. Lu et al. (2020) demonstrated that for both the Longmaxi and Marcellus shale, the effective aperture of fractures had the trend of increasing first and then decreasing with the growth of shearing slip length, and high normal stress can strengthen the decay of fracture permeability. This phenomenon may be attributed to the dilatancy effect at low stress conditions and shearing failure and breakage of surface asperities under high stress and a high sliding rate (Gutierrez et al., 2000). Gensterblum et al. (2015) further measured the conductivities of two types of IU fractures, clay-rich and calcite-rich Haynesville shale, and after surface slippage, the conductivity of clay-rich shale declined substantially while the conductivity of the latter rose up. Zhang et al. (2014) indicated that due to the relatively lower hardness and non-deformability of fracture filling minerals in shale, the conductivity of full-cemented fractures is much less than that of partly filled or unfilled fractures after slippage.

Apart from non-unified testing procedures, the above seemingly contradictory outcomes indicate that the closure and conductivity degradation mechanisms of IU fractures in shale are still not well-understood, particularly reflected in two aspects. One is that organic shale has typical laminated structures and anisotropy, and high stress coupling with diverse surface topography, minerals and meso-structures make the change tendency of IU fractures more complicated. The other is that due to the generation mechanism of IU fractures, these fractures may contact a fracturing fluid or not during a hydraulic fracturing process, and this difference may also cause varied responses of fracture width and conductivity at high closure stress. This paper takes the downhole cores of the Longmaxi shale in the Weirong District of the Sichuan Basin and prepares three types of fractured samples to represent the IU fractures vertical/parallel to the beddings and activated natural fractures. First, based on the high precision laser scan, the fracture spaces of these three types of fractures are reconstructed. Then, the changing trend of a fracture space with the increasing of slipping distance is displayed by applying a numerical method, and the corresponding experiments are conducted to illustrate the differentiated mechanisms of conductivity degradation. Finally, the diverse influences of fracturing fluid treatment on fracture conductivity degradation are deeply investigated, and some useful outcomes are recommended for hydraulic fracturing design and well production modelling.

2. Experimental samples and methods

In this paper, the samples come from the Weirong shale gas district in Sichuan Basin of China, and all samples are downhole cores of Longmaxi Formation shale of the Silurian age, with a burial depth of 3900–4200 m. Mineral composition (wt%) analysis shows that quartz and clay are the dominant minerals and account for about 47% and 38%, respectively, and feldspar (6%), dolomite (4%), calcite (2%) and pyrite (3%) compose the rest part of minerals. The total organic carbon (TOC) of the samples was about 1.95%–3.83%, and the porosity and permeability ranged in 1.22%–3.67% and 0.0007–0.2855 mD.

Considering the scarcity of the downhole cores and the limitations of the experimental facilities, standard core plugs with a diameter of about 2.5 cm and a length of 4.0–5.0 cm were used here. In order to mimic the IU fractures after hydraulic fracturing,

the samples were split with a method similar to Brazilian splitting. As shown in Fig. 1, the core plugs were manually split vertical (MSV, Fig. 1(b)) or parallel (MSP, Fig. 1(c)) to the beddings, on behalf of different types of unpropped fractures induced in the rock mass. The pictures show that for the MSV samples, there exist up and down steps (yellow arrows) caused by the bedding microstructures during the splitting process, and for the MSP samples, there exist obvious horizontal deposits of graptolite, which is well consistent with the sedimentary characteristics of the organic shale. Samples with natural fractures parallel to the beddings (NFP, Fig. 1(d)) were also involved here to represent the activated natural fractures during fracturing.

Surface morphology was the key factor that affected the conductivity of IU fractures, so a three-dimensional laser scanning method was used to obtain high precision location and coordinate information of the fracture surface asperities. The used device (Fig. 2(a)) could record coordinate data at 50 μm intervals in both the x- and y-directions on the planes, and the height of each scanned point (z-direction) was measured with a precision of ±5 μm. Based on the scanning data, we first obtained the cloud picture of each roughness fracture surface, and then the fracture space was computed and reconstructed for both initial aligned fractures and slipped fractures. Then the fractured samples were placed into the core holder to measure their conductivity under varied effective stress (Fig. 2(b) and (c)). In these experiments, samples with aligned fracture faces and slipped fracture faces were used to reflect the conductivity changes under an increasing effective stress of 5–50 MPa. The testing fluid was pure nitrogen (99.9%), and the outlet pressure (back pressure of the downstream) was fixed at 3 MPa so as to weaken the gas slippage effects. The final fracture conductivity was calculated via the following equation:

$$D_f = \frac{2Q_0P_0\mu L}{A\left(P_1^2 - P_2^2\right)}w_f \tag{1}$$

where D_f is the fracture conductivity, $\mu m^2 \cdot cm$; w_f is the average hydraulic fracture width, cm; Q_0 is the flux of the samples, cm^3/s; μ is the nitrogen viscosity at testing conditions, mPa·s; A is the effective section area, cm^2; L is the length of the sample, cm; P_0, P_1, and P_2 are the atmospheric pressure, inlet pressure, and outlet pressure, respectively, MPa.

3. Description of the roughness fracture surface

Three-dimensional laser scanning was implemented for six Longmaxi shale samples here. Due to the impact of the surrounding ambience and non-reflective medium of the surface, the scanned point cloud data body usually existed bits of noisy points. The noisy points were first deleted manually and the remaining tiny empty areas were repaired with Kriging interpolation method (Cai et al., 2013). Then an initial 3D fracture surface was generated, but this geometry may contain invalid points at the base area. We took the lowest point of the fracture surface as the zero-surface, and based on the new reference plane, more concise and precise reconstructed fracture faces were obtained. As displayed in Fig. 3, one fracture surface had about seven to nine hundred thousand points, which can provide sufficient details and reflect the real surface morphology.

As shown in Figs. 3 and 4, the surface contour exists striking difference among the samples. Surfaces split perpendicular to the beddings generally have bigger micro fluctuation than the surfaces parallel to the beddings. Three parameters, root mean square deviation (RMSD), kurtosis coefficient, and dip angle of the asperity, are applied to quantitatively describe the fracture surface morphology (Fig. 3). RMSD is the key parameter to represent the surface discreteness and volatility, and defined as (Liu et al., 2011)

$$S = \sqrt{\frac{1}{mn}\sum_{j=1}^{m}\sum_{i=1}^{n}\left(z(x_i, y_i) - z_0\right)^2} \tag{2}$$

where S is the root mean square deviation, mm; z_0 is the average height of all the points relative to the previous zero reference plane, mm; $z(x_i, y_i)$ is the height of the point which has coordinates of x_i and y_i, mm; m and n mean the total data points in the x- and y-directions.

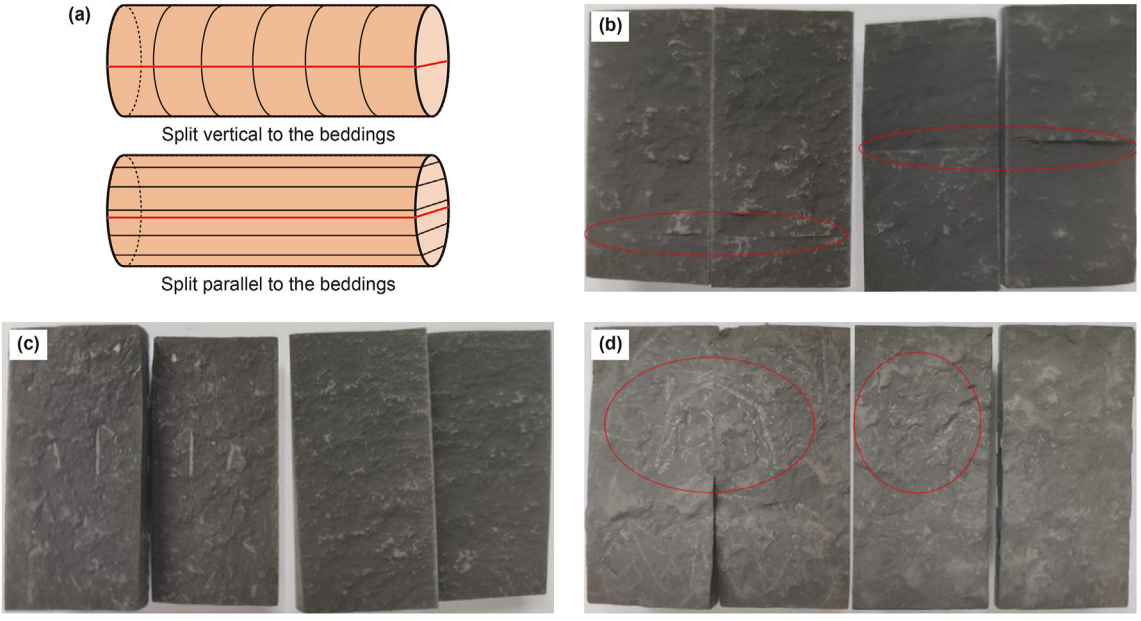

Fig. 1. Schematic diagram and images of the fracture surfaces. (**a**) Relations between the split orientation and shale beddings; (**b**), (**c**) Fresh fracture surfaces of manually split vertical/parallel to the beddings; (**d**) Aged surfaces of natural fractured samples. The fracture planes were also approximately parallel to the beddings.

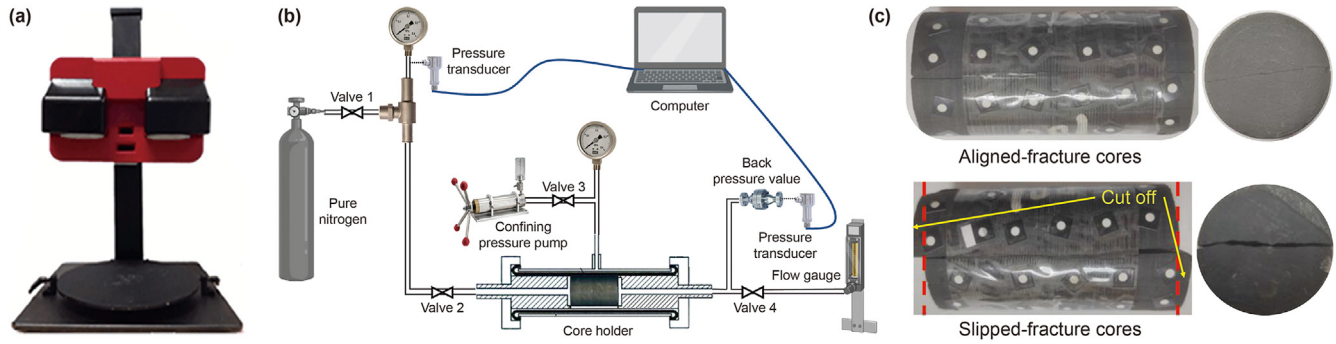

Fig. 2. Experimental setup and samples. (**a**) 3D laser scanner; (**b**) Equipment for fracture conductivity measurement; (**c**) Representative sample before and after fracture surface slippage.

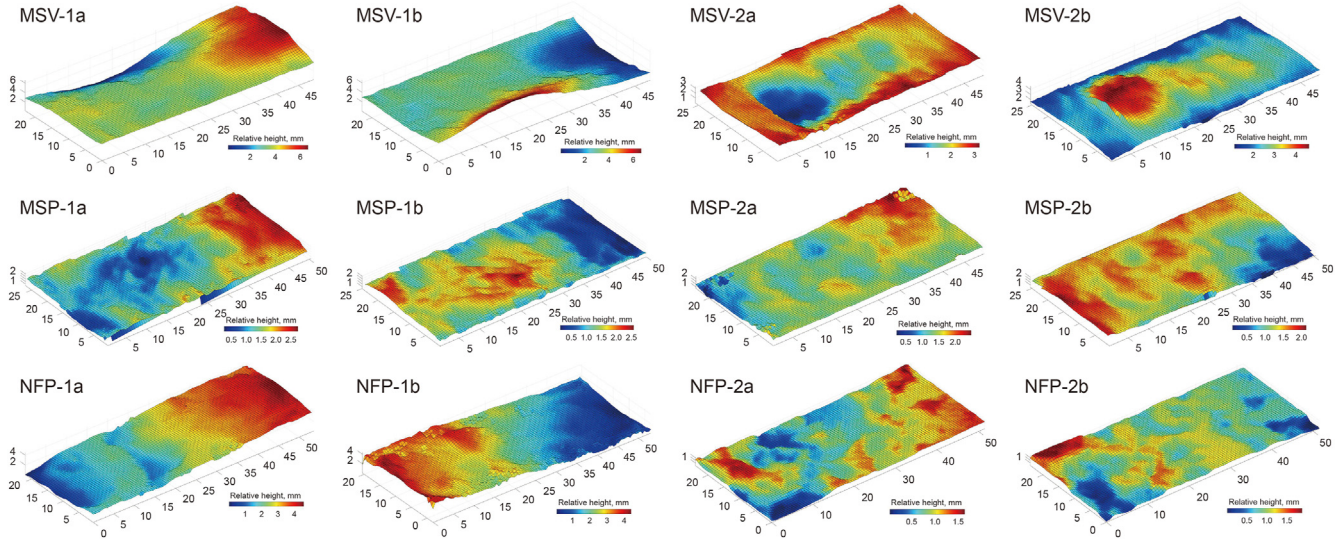

Fig. 3. Scanning images of the individual surface of the split shale plugs (a and b respectively mean the upper surface and lower surfaces).

Kurtosis coefficient mainly reflects the convex degree of the height contour or the dispersion or concentration degree of the distribution probabilities and can be written as (Fan et al., 2012)

$$b_k = \frac{1}{S^4 L}\int_0^L [z(x_i, y_i) - z_0]^4 \mathrm{d}x \tag{3}$$

where b_k is the kurtosis coefficient (dimensionless); L is the sample length along with the x-axis direction, mm. Generally, $b_k = 3$ denotes that the height of the scanned points obeys normal distribution, and $b_k < 3$ means the height distribution is more dispersed while $b_k > 3$ means the distribution is more concentrated. The asperity dip angle is another significant parameter to describe the surface roughness, and it is defined as

$$\theta = \frac{1}{n}\sum_{i=1}^{n} \arctan\left(\frac{z_i - z_{i-1}}{l_i - l_{i-1}}\right) \tag{4}$$

where θ is the average dip angles of the surface asperities, °; n is the number of analytical units or the number of asperities; z_i and l_i are the height and horizontal distance to the reference point, mm.

Based on the above equations, we compute the key parameter of all six fractured samples. Table 1 demonstrates that compared with the horizontal fracture faces, the split surfaces vertical to the beddings have bigger values in all three terms. Higher RMSD values mean that the surface elevation of MSV samples changes more dramatically, for instance the macro fluctuation and micro asperity altitude difference. The calculated kurtosis coefficient is 4.05 (bigger than 3.0), and the average dip angle is about 12.52°. All three parameters indicate that for the MSV samples, the height of surface asperities distributes intensively in a relatively bigger value scope, and the shape of the asperities seems very sharp, which may lead to excessive stress concentration on the asperities and is not conducive to withstanding high stress loads (Dam et al., 2000; Fredd et al., 2001; Ban et al., 2018).

The RMSD values of MSPs and NFPs are relatively small due to the controlling effects of the horizontal bedding microstructures of shale. The kurtosis coefficients of the four samples are all below 3.0 and the asperity dip angle is about 6.28°–8.12°, meaning that the asperity heights distribute dispersedly and their shapes are gentle and blunt, which may be conducive to withstanding high closure stress. Comparing the manual and natural horizontal fractured samples (Table 1 and Fig. 1), we may find some tiny but interesting differences that the NFP samples have bigger RMSD and dip angles but smaller kurtosis coefficients. The reason may be attributed to the heterogeneous dissolution under in-situ conditions for the NFP samples. This effect may randomly strip soluble minerals and leave hard minerals along the natural fracture planes (Dieterich et al., 2016; Zeng et al., 2022), which can enlarge the elevation difference of the tiny bumps and depressions. This makes the asperity

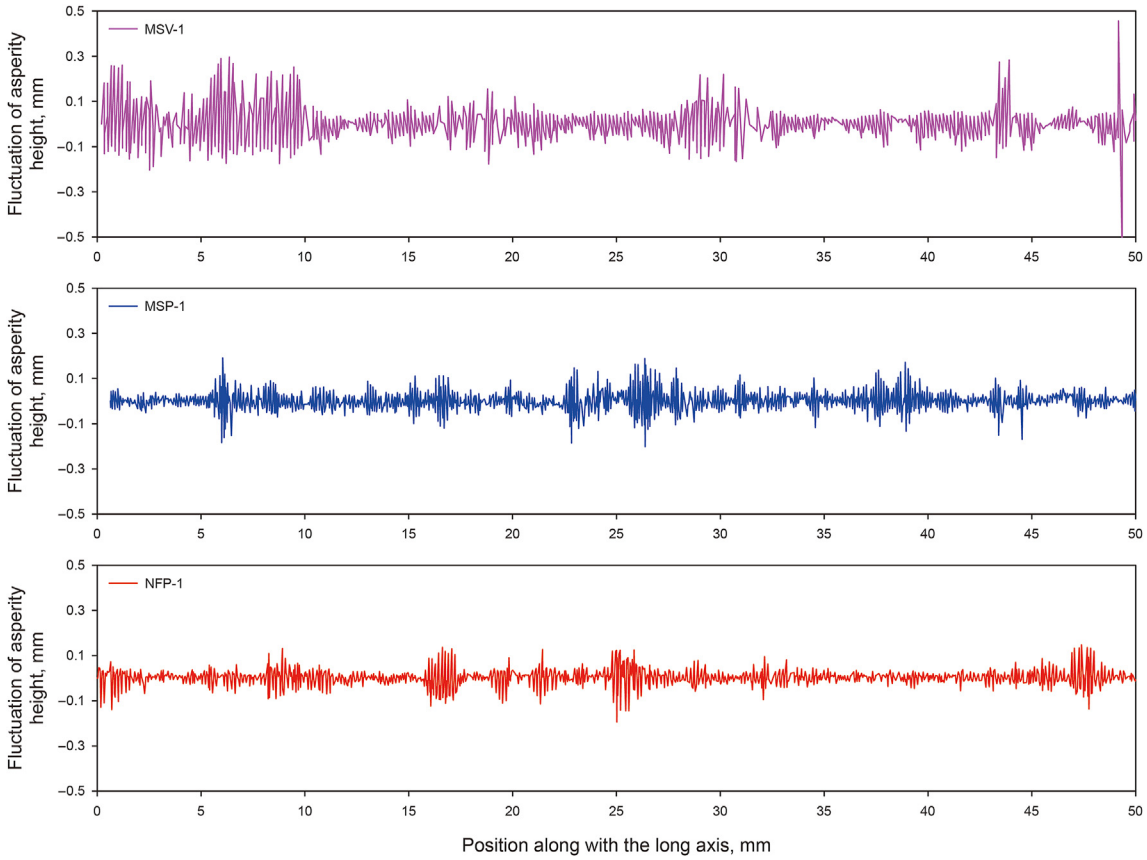

Fig. 4. Fluctuation of surface asperity height along with the long axis direction.

Table 1
Surface morphology parameters of the fractured samples.

Sample	Original			Stress aged		
	S, mm	b_k, dimensionless	θ, °	S, mm	b_k, dimensionless	θ, °
MSV-1	1.09	4.16	11.84	0.64	3.56	6.74
MSV-2	0.94	3.94	13.20	0.67	3.34	7.55
Average	1.02	4.05	12.52	0.655	3.45	7.15
MSP-1	0.53	2.45	8.12	0.38	2.12	6.78
MSP-2	0.44	3.37	6.28	0.34	2.85	5.43
Average	0.485	2.91	7.20	0.36	2.485	6.11
NFP-1	1.02	1.92	7.71	0.58	1.75	6.37
NFP-2	0.48	2.75	6.97	0.31	2.27	6.19
Average	0.75	2.335	7.34	0.445	2.01	6.28

height distribution deviate from the normal distribution and become more dispersed, and finally leads to the increasing of RMSD and θ values and the decreasing of b_k.

4. Fracture space analysis of the slipped fractures

4.1. Reconstruction of the fracture space

The conductivity of IU fractures comes from the surface roughness and self-propping of the asperities. The previous section obtained the morphology information of fracture faces, and this section would reconstruct the fracture space before and after fracture displacement. First, it needs to define the height matrices of surface asperities as follows:

$$\begin{cases} A_0 = (a_{0ij}), \ \ (i = 1,2,3,\ldots,m;\ j = 1,2,3,\ldots,n) \\ A_1 = (a_{1ij}), \ \ (i = 1,2,3,\ldots,m;\ j = 1,2,3,\ldots,n) \end{cases} \tag{5}$$

where A_0 and A_1 are the upper and lower surface matrix, respectively. Then several key steps, including substrate removal, symmetric placement, mis-alignment movement, and double-wall single-point contact (Lu et al., 2020), are needed to finish this reconstruction. As mentioned above, the lowest point of the fracture surface is assumed as the new reference plane, and all the grid data are updated by subtracting the height of the new reference plane.

$$\begin{cases} A_0' = \left(a_{0ij}'\right) = \left[a_{0ij} - \min\left(a_{0ij}\right)\right], \ (i = 1,2,3,\ldots,m; j = 1,2,3,\ldots,n) \\ A_1' = \left(a_{1ij}'\right) = \left[a_{1ij} - \min\left(a_{1ij}\right)\right], \ (i = 1,2,3,\ldots,m; j = 1,2,3,\ldots,n) \end{cases} \tag{6}$$

During the surface scanning experiments all fractures are placed face up, so here the upper fracture faces need to be reversed vertically and describe mathematically as (Fig. 5(a))

$$A_{0R}' = \left(a_{0Rij}'\right) = \left[a_{0ij}' - \max\left(a_{0ij}'\right)\right], \ \ (i = 1,2,3,\ldots,m;\ j = 1,2,3,\ldots,n) \tag{7}$$

Then the highest value of the lower surface is added to the reversed matrix of the upper surface to get the symmetrically placed matrix. Meanwhile, the lower surface matrix remains unchanged (Fig. 5(b)).

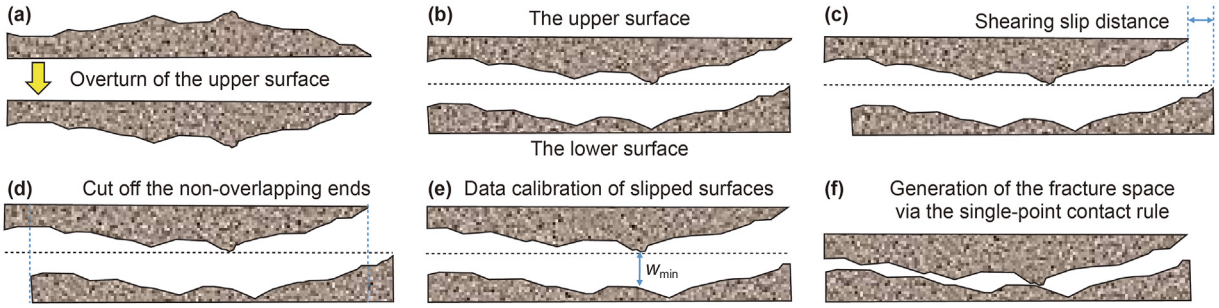

Fig. 5. Schematic diagram of the reconstruction of the slipped fracture space.

$$\begin{cases} A_{0S}=(a_{0Sij})=\left[a'_{0Rij}+\max\left(a'_{1ij}\right)\right], (i=1,2,3,\ldots,m;j=1,2,3,\ldots,n) \\ A_{1S}=A'_1 \end{cases} \tag{8}$$

The generation of IU fractures usually accompanies by the shearing sliding of the fracture planes, so relative displacement of the surfaces is also needed to reconstruction the fracture space after slippage (Briggs et al., 2014). As shown in (Fig. 5(c) and d), by fixing the lower fracture surface and moving the upper one, the misaligned movement is carried out along the long axis direction, and after this displacement the height matrices of the upper and lower fracture surfaces are rewritten as

$$\begin{cases} A_{0SDIS}=\left(a_{0SDISi(j-c)}\right)=(a_{0Sij}),\ \ (i=1,2,3,\ldots,m;\ j=d,d+1,d+2,\ldots,n) \\ A_{1SDIS}=(a_{1SDISij})=\left(a_{1Si(j+c)}\right),\ \ (i=1,2,3,\ldots,m;\ j=1,2,3,\ldots,n-d) \end{cases} \tag{9}$$

where c is the relative displacement of the upper and lower surfaces, mm. Under in-situ conditions, the maximum fracture space appears when the two points which have minimum vertical distance (w_{min}) just become in touch (Gou, 2017). By subtracting w_{min} from the upper fracture face (Fig. 5(e) and (f)), a group of newly height matrices of the upper and lower surfaces are obtained again.

$$\begin{cases} Z_u=\left[a_{0SDISij}-\min(a_{0SDISij}-a_{1SDISij})\right],\ \ (i=1,2,3,\ldots,m;\ j=1,2,3,\ldots,n-d) \\ Z_d=A_{1SDID} \end{cases} \tag{10}$$

where Z_u and Z_d are the newly upper and lower surface matrix, respectively. Taking Eqs. (5)–(10), we can reconstruct the fracture space of slipped samples, and by assuming $d=0$, the fracture space of originally split sample can also be obtained.

4.2. Variation character of the slipped fracture space

Fig. 6 displays the initial 3D fracture space of the reconstructed samples. For both the newly split and the natural fractured samples, there exist obvious fracture space even though the upper and lower faces align well under no-slipping conditions. This is mainly because during the generation of the fractures the microscale deformation and breakage of the surface have occurred in spite of the macroscale alignment. It seems that the NFPs have the largest fracture space, and this may be explained that during the long-term geological process, the surfaces of natural fractures have suffered remarkable long-term geological process dissolutions, while the fresh split surfaces of MSVs and MSPs can gear with each other well. It should also be emphasized that at initial stage of the manually split fractures, with no slippage, the fracture space has no necessary correlations with the surface asperities. Only when the slippage occurred, the surface topography and asperity features become one of the dominant factors that determines the fracture spaces. More details about the fracture width and conductivity will be discussed later.

Under in-situ conditions, the majority part of IU fractures would go through a slippage process, and this may greatly affect the fracture space and conductivity (Fredd et al., 2001; Zhang et al., 2014). About the specific slipping distances for different shale formation, many researchers (Zhao et al., 2012; Guo et al., 2013) obtained varied values, in a wide scope of 2–15 mm. In this paper, we take a maximum slipping distance of 8 mm and an interval of 1 mm to numerically analyze the fracture space changes via the method in Section 4.1. Meanwhile, in order to quantitatively and concisely describe the sample fracture width changes along with the increasing of slipping distance, a weighted average fracture width of the samples is defined

$$w_{aver}=\frac{1}{A}\sum_{i=1}^{N}A_i w_i \tag{11}$$

where A_i is the area which have a fracture width of w_i; A is the total surface area.

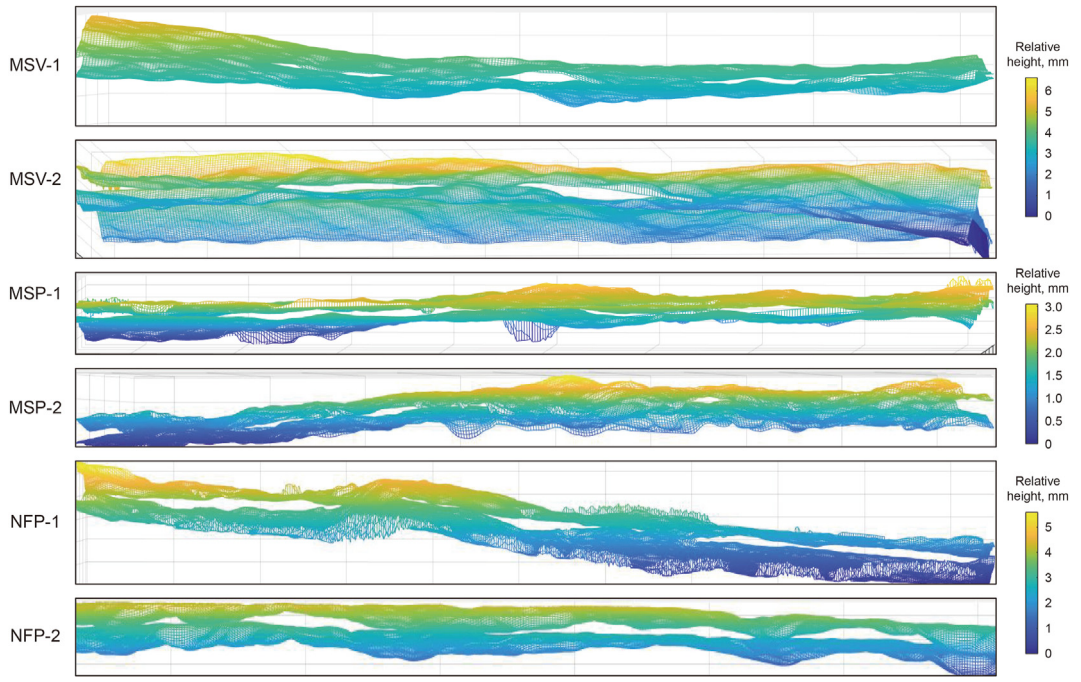

Fig. 6. The initial 3D fracture space of the samples.

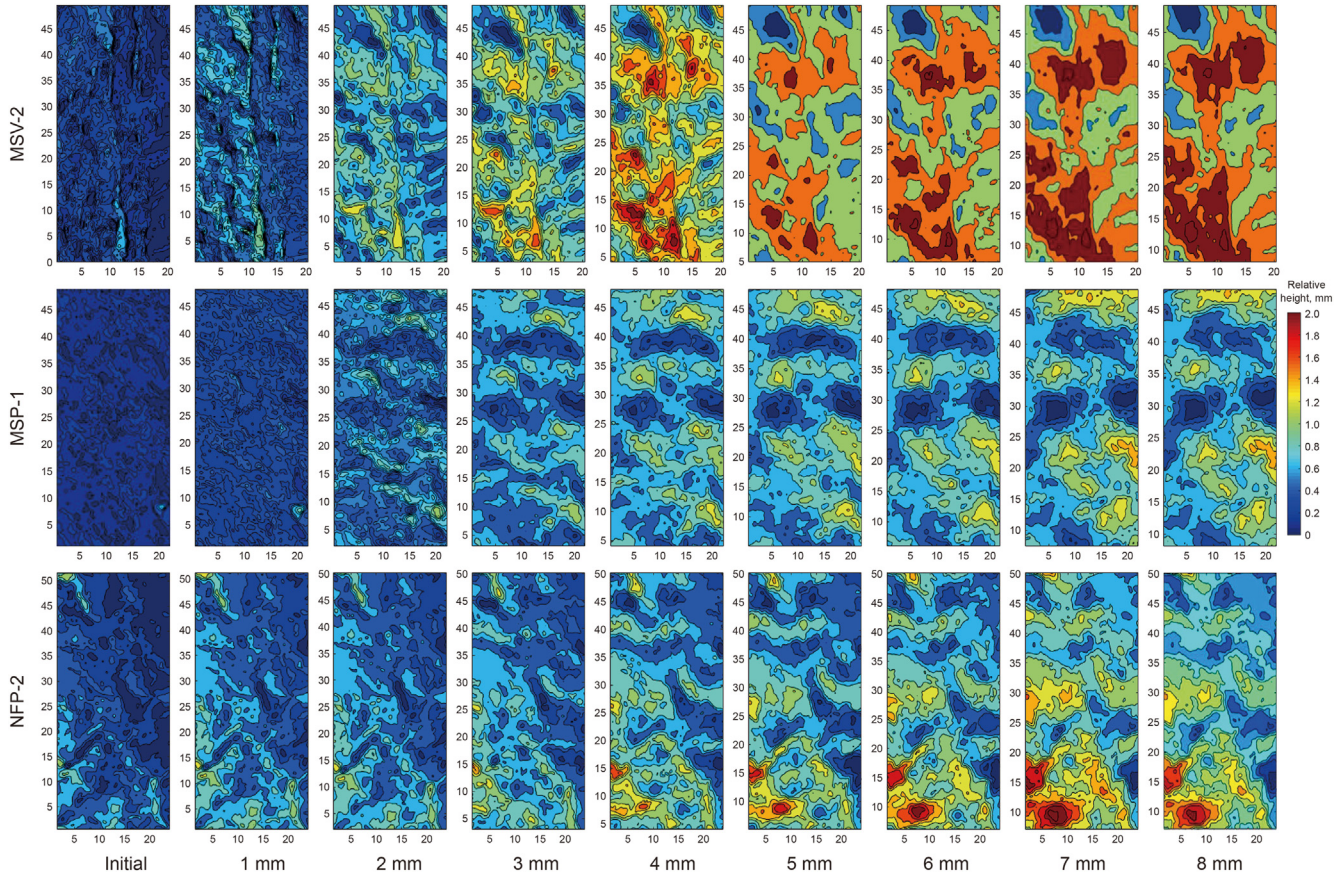

Fig. 7. The fracture width changes along with the increasing of slipping distance (partly pictures).

Fig. 7 clearly demonstrates that with the growth of slipping distance, the fracture width increases remarkably, and the rougher surfaces, such as the MSV samples, have bigger fracture width increments. Taking Eq. (11), the average fracture width is also

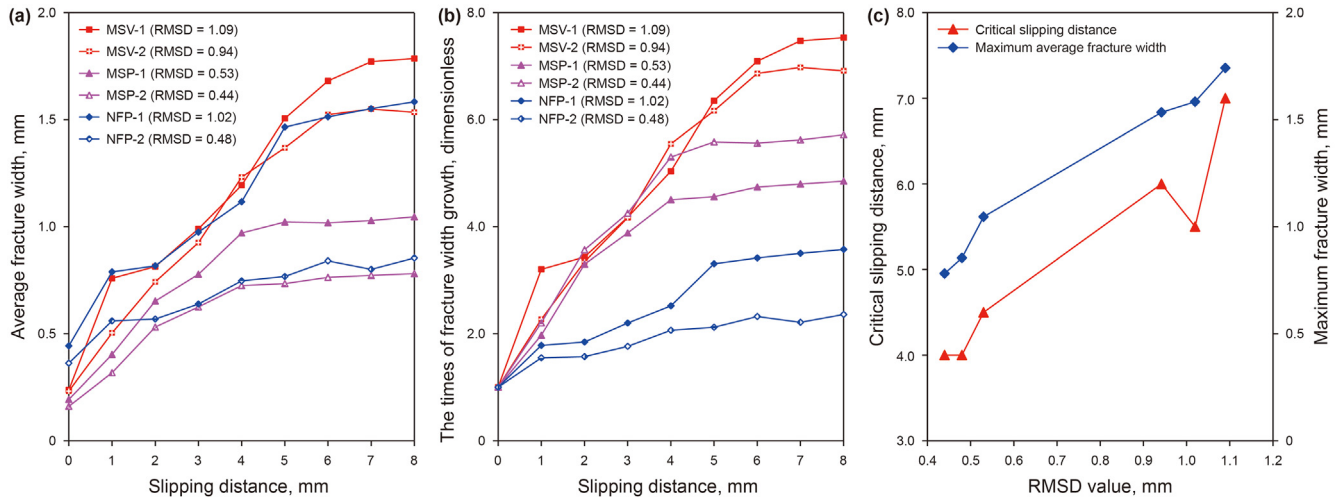

Fig. 8. Evolution characteristics of the slipped fractures. (**a**) Average fracture width versus slipping distance; (**b**) The times of fracture width growth versus slipping distance; (**c**) The maximum fracture width versus RMSD values.

computed. As shown in Fig. 8, the NFP samples have the biggest initial fracture width (0.362–0.443 mm) since the natural fracture surfaces have gone through long-term geological process (Zeng et al., 2022) and the upper and lower faces cannot gear with each other well. As for the newly split samples, the fracture faces can match well so that the initial fracture width of MSV and MSP samples are merely 0.161–0.193 and 0.232–0.237 mm, respectively. When the surface slippage occurs, the fracture width of all samples appears remarkable growth at early stage, and then reach the plateau stage. Here we define the slipping distance corresponding to the starting point of the plateau stage as the critical slipping distance (d_c), and this critical value ranges 4–7 mm, in the increasing sequence of MSPs, NFPs and MSVs on the whole. The maximum fracture width after slippage (w_{smax}) of the samples is about 0.73–1.79 mm, which accord well with the previous surface roughness features (Fig. 4 and Table 1) and the literature (Fredd et al., 2001; Sakaguchi et al., 2006).

Fig. 8 also displays some interesting changes before and after the fracture surface slippage. From an overall perspective, the changes of fracture width versus slipping distances may be divided into two or three stages. For the artificial fractured samples (MSVs and MSPs), two stages may be more suitable. In the first stages, the fracture width increased rapidly along with fracture slipping and then became stable after exceeding a critical slipping distance. For the natural fracture samples (NFPs), the fracture width also increased quickly at the initial slipping process, but then grew relatively slow and finally became stable, so the curves can be divided into three stages. NFP samples have the biggest initial fracture width, however, the average net increment of fracture width follows the order of MSV, NFP, and MSP samples (Fig. 8(a)). Meanwhile, the times of fracture width increment range in a clear order of MSV, MSP, and NFP samples (Fig. 8(b)). Fig. 8(c) shows that the maximum fracture width after slippage is strictly positive correlated with the RMSD values which represent surface roughness and the degree of asperity height volatility, and the correlation between critical slipping distance and RMSD values also follows a similar pattern. The above results indicate that the surface morphology and fracture type have direct influences on the fracture space as well as its evolution tendency. At the same time, they may give some engineering enlightenments that for the natural fractures in shale stratum, just activating the fractures may provide sufficient conductivity, while for the newly generated IU fractures during hydraulic fracturing, high injection rate and strong stress perturbation may need to induce enough fracture slippage and obtain high conductivity (Lu et al., 2021).

5. Conductivity degradation of the un-propped fractures

5.1. Fracture conductivity under high stress

The above contents describe the features of the fracture surfaces and corresponding reconstructed space at stress-free conditions, and this section would explore the evolution of the fracture space as well as conductivity at high closure stress conditions. The fracture conductivity of the displaced samples is measured using the experimental setup and procedures in Section 2, and we take the above critical slipping distance ($d_c = 4–7$ mm) which is close to the distance in other experimental and simulative works (Zhao et al., 2012; Lu et al., 2022) as the dislocation distance of the tested samples. Fig. 9 displays that compared with the no-slip fracture samples, the conductivity of the displaced samples rises by two to four orders (Zou et al., 2013; Zhang et al., 2014). The results verify that the dislocation and subsequent mutually propping of the asperities significantly enlarge fracture flow space even under high closure stress, consistent well with the previous fracture space prediction of slipped samples. Moreover, although the initial conductivity of the three types of fractured samples varied in a huge scope under no-slip conditions, the fracture conductivity gap is largely narrowed after slippage, generally in the same order of magnitude, which indicates that the presence and mismatch of the surface asperities have determinant influences on fracture conductivity (Fredd et al., 2001).

Fig. 9(a) also provides plenty of details to reveal the flow conductivity differences of the three types of fractures. For the new-manually split fractures, the height of surface asperities contributes more to the fracture flow capacity under initial and low closure stress conditions (< 15 MPa), so the conductivities of MSVs are higher than those of MSPs. As the closure stress grow up, the strength, dip angles, and distribution of the asperities become more important. As shown in Figs. 1 and 4, the asperities of the MSV samples appear to be lamellar and sharp, and tend to encounter huge stress concentration. Meanwhile, the strength of the lamellar asperities is relatively small, and the surface asperities would suffer large-scale plastic deformation and breakage. Oppositely, the

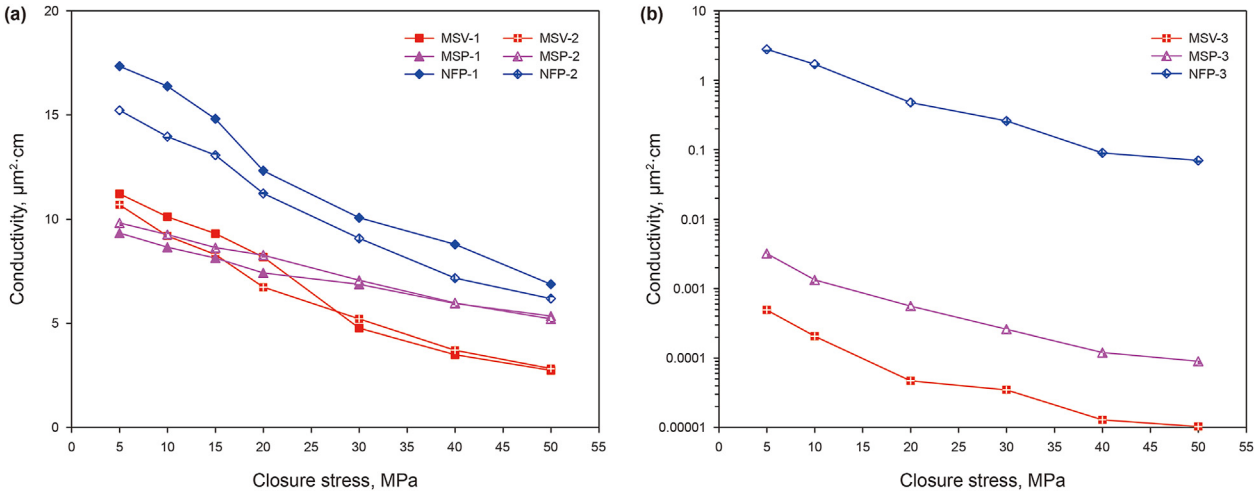

Fig. 9. Fracture conductivity via increasing closure stress. (**a**) Slipped fracture samples; (**b**) Original no-slip fracture samples.

asperities of the MSP samples appear to be dispersive with gentle slopes (Table 1), so the stress concentration and consequent asperity crush would be weakened. As a result, the MSPs reversely maintain bigger conductivities under high stress conditions. With respect to the natural fractures (NFPs), the surface asperities have relatively scattered and gentle slopes (Table 1). Moreover, these natural fracture surfaces have gone through long-term geological process, the preserved asperities usually compose of hard minerals and have relatively big strength. So NFPs maintain the biggest fluid conductivity.

5.2. Mechanical mechanism of conductivity degradation

Assuming the sample conductive space as a slab fracture, the average hydraulic fracture width can be computed according to the cubic law (Witherspoon et al., 1980). As shown in Fig. 10, the initial fracture width after surface slippage (from Fig. 8(a)) ranges from 724.8 to 1231.5 μm under stress-free conditions, and when the closure stress is exerted on the fractures, the calculated average hydraulic fracture width sharply falls to 69.0–127.7 μm. The residual fracture width is about 8.7–10.7 percentages of the initial stress-free fracture width, smaller than the residual fracture width proportion (15%–30%) of tight sandstone (Warpinski et al., 1997) and artificial rocks (Dam et al., 2000), and this diversity may be attributed to the differences of rock roughness and strength. Then as the closure stress rises from 5 to 50 MPa, the fracture width further declines and the decrement follows the order of MSVs (35.9%–37.5%), NFPs (25.0%–26.6%), and MSPs (17.1%–19.1%), which means the MSV fractures have the strongest stress sensitivity and the MSPs have the weakest stress sensitivity. Two main reasons may be responsible for this conductivity degradation tendency.

One is the mineral composition and microstructure of the fracture contact faces. Fig. 11 displays the images of the scanning electron microscope (SEM) and mineral contents detected by energy disperse spectroscopy (EDS) of the three types of fracture surfaces. These images clearly show the differences of surface appearance and mineral contents. Due to the bedding structures of shale, the MSV sample appears to be coarse and cracked, and exists plenty of bedding fractures, while the surfaces paralleling to the beddings (MSP and NFP) seem to be smooth. Meanwhile, the newly split surface (MSV and MSP) is neat and tidy, but the natural fracture surface (NFP) has obvious mineral corrosion and sediment

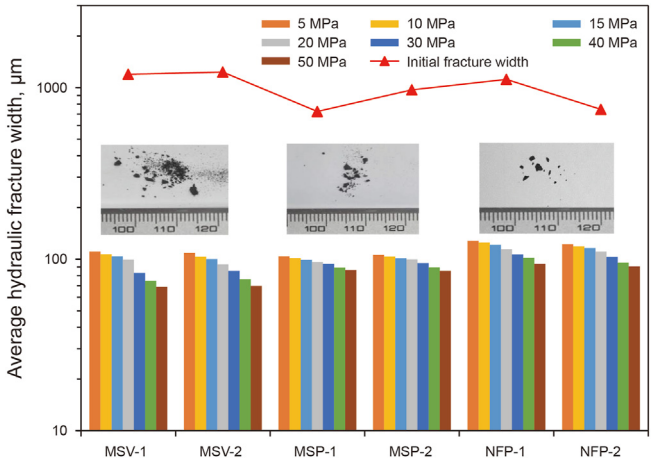

Fig. 10. Change tendency of the fracture width with increasing closure stress.

which occurred in a long geological process. The histogram in Fig. 11 shows that the carbonates proportion (22.7%) of natural fracture surface is much larger than the newly split surfaces, and oppositely, the clays and quartz contents of natural fracture surface are remarkably lower than those of newly split surfaces. EDS of the natural fracture surface verifies that the main component of the deposits is calcite, a commonly fracture filling mineral in shale (Dieterich et al., 2016; Shi et al., 2019), and this filling calcite as well as its relatively lower strength compared with quartz and feldspar may partly explain why the stress sensitivity of NFPs is stronger than that of MSPs in Fig. 10.

Another is the strength anisotropy of the fracture contact faces. Micro-indentation experiments are conducted to detect the surface strength, paralleling and vertical to the beddings (Fig. 12). Detailed testing and calculating procedures can be found in previous literature (Oliver and Pharr, 1992; Chen et al., 2015; Shi et al., 2019; Jia et al., 2021). The results show that the elastic modulus and hardness of the fracture surfaces range 23.7–44.1 GPa and 1.16–1.89 GPa, respectively. The values are very close to results obtained by other literatures for Longmaxi shale with micro-indentation (Chen et al., 2015; Dong, 2018), and slightly smaller than the results obtained with nano-indentation which may be attributed to the size effect and micro heterogeneity of the mineral distribution (Shi et al., 2019; Jia et al., 2021). Moreover, our results

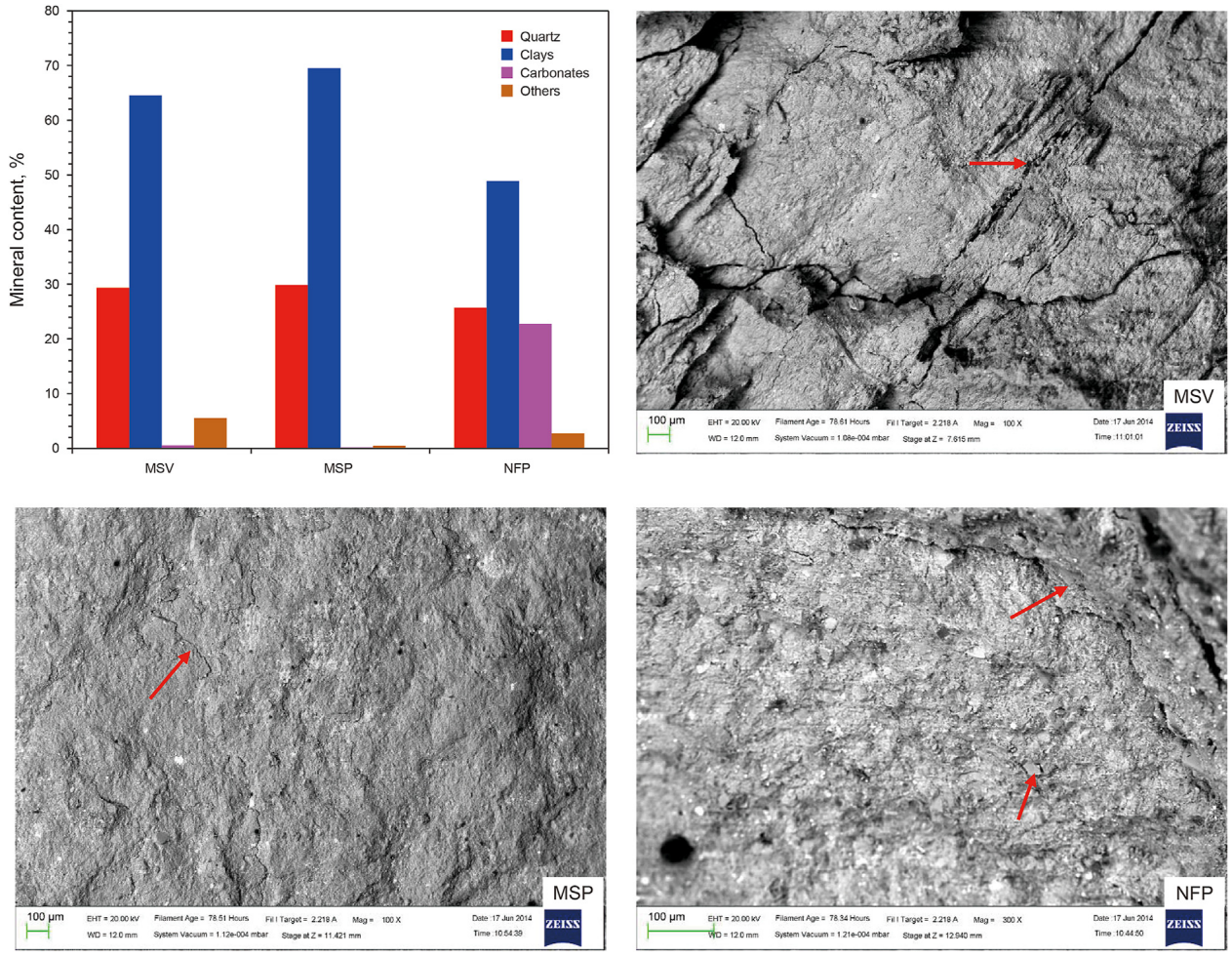

Fig. 11. SEM images and corresponding mineral contents detected by EDS.

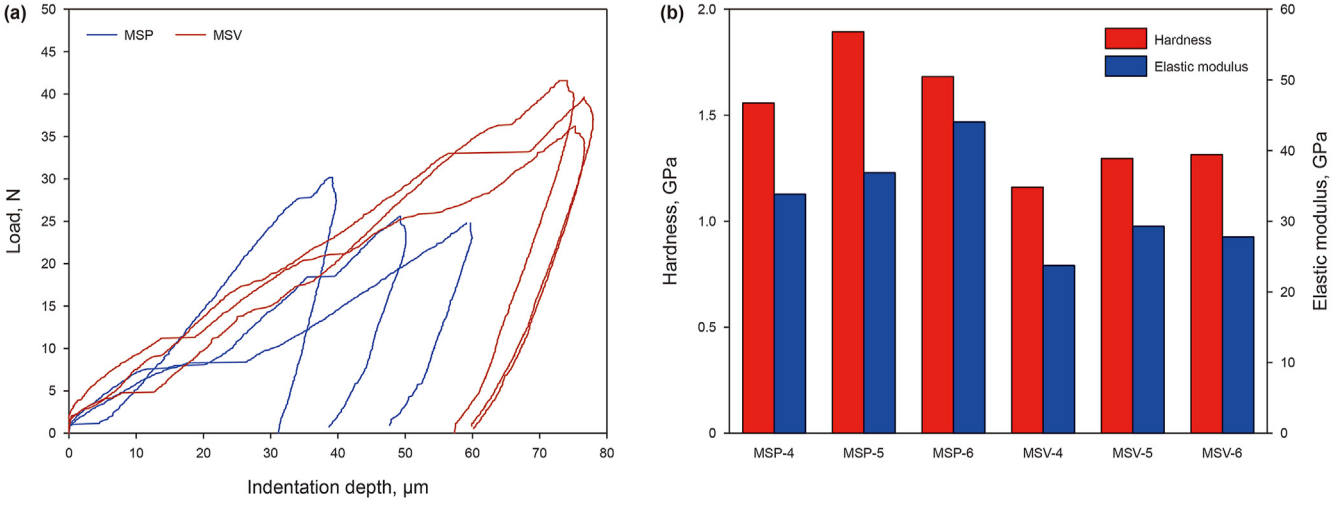

Fig. 12. Strength analysis of the fracture surfaces via micro-indentation experiments.

as well as other literature demonstrate that compared with MSV samples, the fracture surfaces paralleling to the beddings (MSP) have higher modulus and hardness (Dong, 2018; Shi et al., 2019), and the anisotropic difference is about 3.5%–31.6%. The main reason that contributes to the relatively lower modulus and hardness of MSV samples may be the cracked surface (Fig. 11), and during the contacting and compacting process, the surface asperities can easily knock in the bedding fractures and lead to the breakage of the vertical thin layers structure.

Fig. 13 displays the asperity height of fracture surfaces before

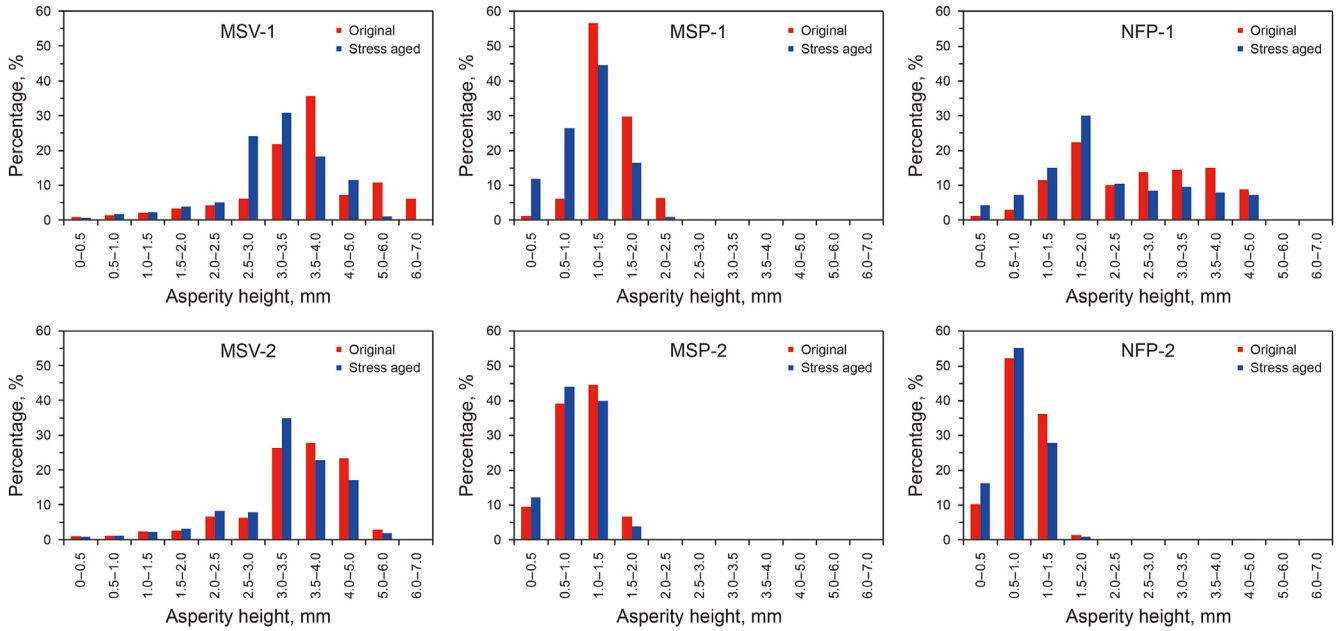

Fig. 13. Changes of surface asperity height (relative to the zero-surface) after stress treatment.

and after high-stress conductivity tests based on the method in Section 3. Undergoing the surfaces contact, deformation and breakage process (stress aging), all samples present a uniform change trend that the proportion of asperities with higher altitude decreases and inversely the proportion of lower altitude asperities increases, and the surface morphology parameters (RMSD, kurtosis coefficient, and dip angle) all decrease to smaller values (Table 1). This is because the high and sharp asperities suffer the major part of closure stress and occur irrecoverable deformation or breakage, and consequently the height of these asperities are cut down and more asperities become blunt. Moreover, interesting differentiation can also be found in the three types of fracture surfaces. The changes of asperity height of MSVs are most remarkable due to the extensive deformation and broken, for example the broken particles and powders in Fig. 10. The NFPs have secondary stress sensitivity, but the surface asperity breakage reflected by the quantity of broken particles (Fig. 10) is quite limited. The relative soft deposits of the natural fracture surfaces, which is more likely to generate plastic deformation instead of breakage during high closure stress, may explain the asperity broken features of the NPFs.

5.3. Influences of fluid treatment on fracture conductivity

During hydraulic fracturing operations, the fracturing fluid (FF) may invade into the induced un-propped fractures, and the consequent fluid imbibition and shale–water interaction during shut-in period can obviously change the surface mechanical properties and impact the fracture conductivity, the permeability of shale rock is directional or anisotropic for shale rock (Liu et al., 2024). For the above three groups of samples, after soaking for 48 h in fracturing fluid (80 °C), the fracture conductivity is measured again with the same testing conditions. As shown in Fig. 14, the conductivities of all six samples appear big drops, and the reduction is about 29.8%–61.7% under 30–50 MPa closure stress. Unlike the previous conductivity change tendency of dry samples, the MSP samples have the most significant conductivity decrement after fracturing fluid treatment, then followed by MSV and NFP samples. Clay mineral hydration of shale and

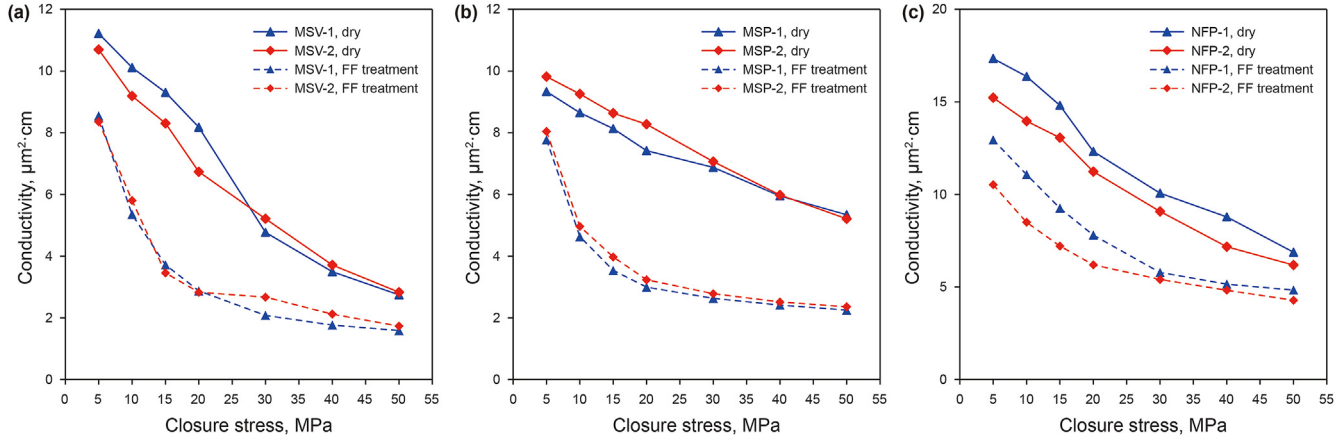

Fig. 14. Fracture conductivities before and after fracturing fluid (FF) treatment.

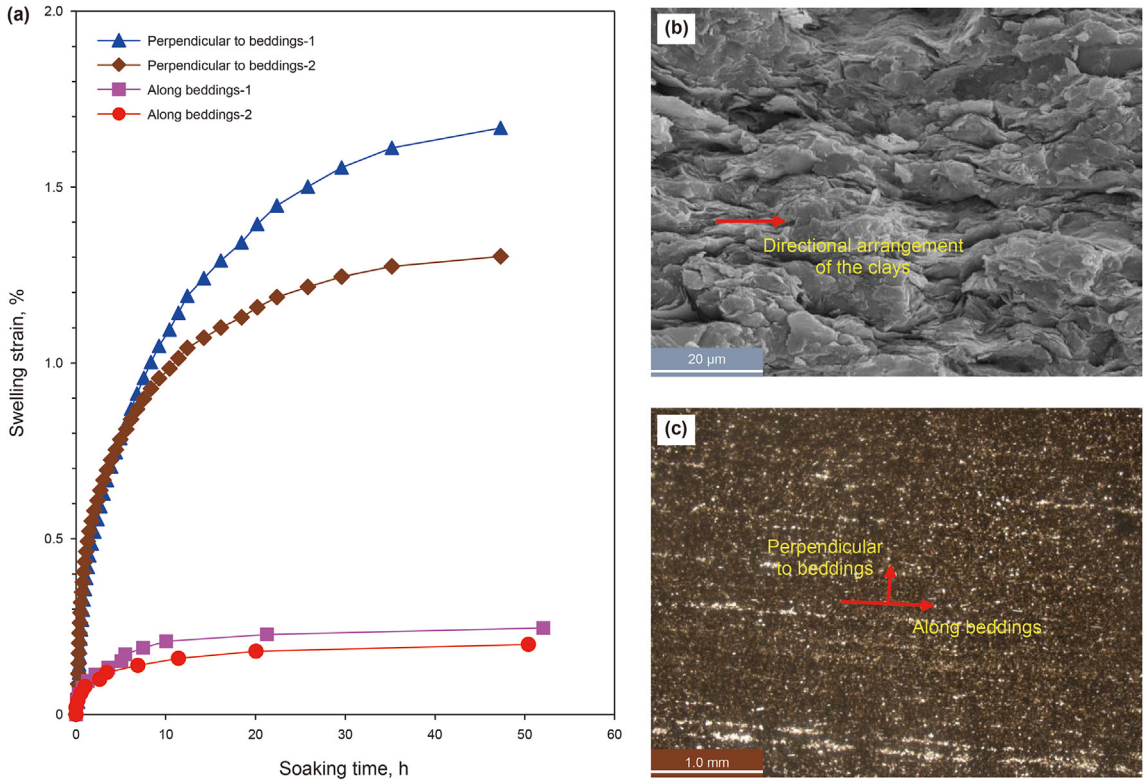

Fig. 15. Hydration swelling anisotropy of shale and the corresponding structure features. (**a**) Swelling strains versus time under fracturing fluid soaking; (**b**) SEM image showing directional arranged clay minerals; (**c**) Mesoscopic laminar structures of rock slice.

corresponding mechanical strength weakness during fluid soaking aer regarded as the main reasons for the aggravation of stress sensitivity (Kang et al., 2017).

Apart from the above reason, the mineral and microstructure features of the fracture surfaces also contribute to the varying degrees of conductivity stress sensitivity. As previous literature (Oliver and Pharr, 1992; Kang et al., 2017; Jia et al., 2021) has revealed that the organic shale has typical laminated structures due to the horizontally directional arranged clay minerals, and this micro-anisotropic feature can cause quite differential failure of hydration. Fig. 15(a) shows that the tested shale samples have remarkable anisotropic swelling strains, and the average strain perpendicular to the beddings is about 1.49%, almost seven times as much as the values along the beddings, and similar results have also been observed by other researchers (Ewy and Stankovic, 2010; Minardi et al., 2018). Fig. 15(b) and (c) display that the mesoscopic laminar structures and microscopic flake-like clays, and according to the DLVO theory and clay hydration mechanism (Kang et al., 2017), the hydration repulsive force can cause obvious expansion between the clay mineral crystal layers, and then lead to macro swelling while shale interacts with fracturing fluid or other water-based fluids. As the micro crystal expansion mainly occurs in the direction perpendicular to the oriented direction of the clay minerals, the macro hydration swelling strain of shale would also be greatly larger in the same direction. Consequently, micro-structure failures and mechanical strength weakness are more likely to occur in this preferred swelling direction if the fracturing fluid invaded or be trapped in shale fractures, and this may explain why the MSP samples have the strongest stress sensitivity after fracturing fluid treatment.

With respect to the relatively low stress sensitivity of NFP samples after interacting with the fluid, the main reason may be attributed to mineral composition changes of the natural fracture surfaces. As demonstrated in Fig. 11, benefitting from the long-term geological process, the clay mineral content of the NFP surfaces has remarkably decreased, compared with the newly split surfaces, and meanwhile high strength minerals like quartz and feldspar are retained. More carbonate mineral deposits and adheres to the surfaces, which may screen water uptake and weaken shale hydration. Finally, the surface mechanical strength of the NFP samples is preserved to some extent, and diminishes the stress sensitivity of fracture conductivity.

5.4. Field enlightenment

For the multi-scale fractured shale gas wells, the IU fractures are the secondary elements to form an artificial fracture network, and act as bridges between primary hydraulic fractures and matrix pores (Fig. 16). Above analyses have elaborated that the unpropped fractures have different surface topography, enclosed space, mineral composition, and mechanical properties. Therefore, their conductivity evolution responds to fracture surface slippage, closure stress, and shale–fluid interactions have obvious differences in terms of change tendency and governing factors, which may need to be considered in both preliminary fracturing design and post-fracturing evaluation. For instance, figuring out the relations between fracture conductivity and slipping distance may help the engineers to obtain the optimal fracture conductivity in an economic way during hydraulic fracturing process. During post-fracturing and production periods, shale–fluid interactions and

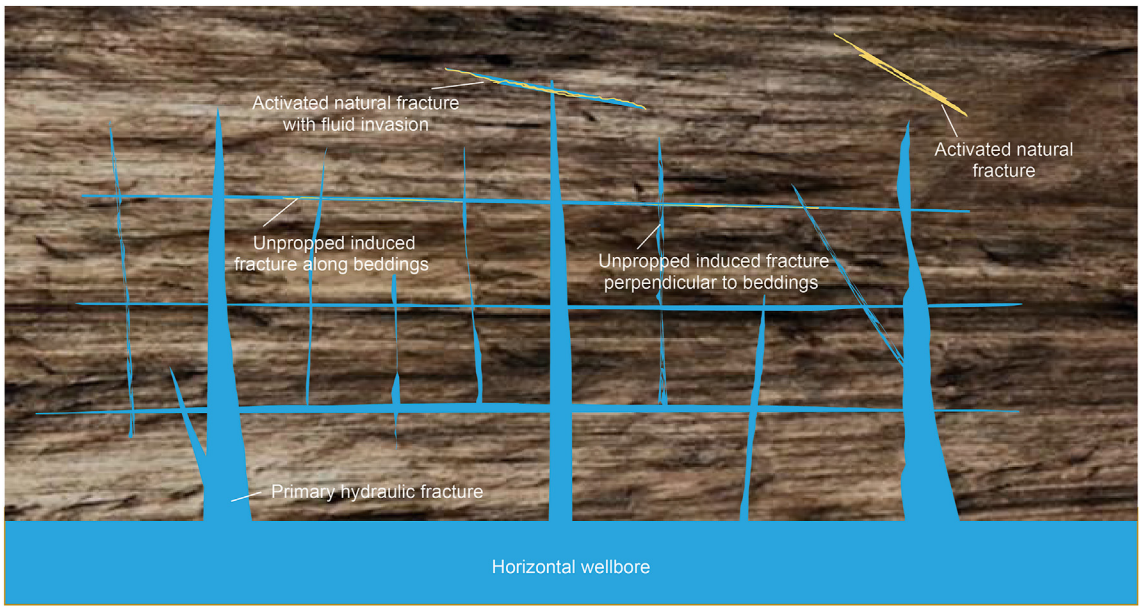

Fig. 16. Schematic diagram of the fracture networks after hydraulic fracturing in gas shale.

fracture stress sensitivity exist persistently, uncovering conductivity degradation trend of different types of unpropped fractures can provide reliable parameters for post-fracturing evaluation and well productivity model, so as to accurately describe the contributions of varied fractures to the total gas production and predict well production decline trend.

6. Conclusions

Three types of induced unpropped (IU) fractured samples are analyzed via the combination of 3D laser scan and fracture space reconstruction techniques. It realizes the refined description of the surface topography and the visualization of the fracture enclosed space, which helps to explore the evolution trends of fracture surface topography and flow conductivity with respect to the fracture slippage, closure stress, and fluid treatment. Fracture space characterization and conductivity evolution analyses allow drawing the following conclusions.

(1) The root mean square deviation (RMSD), kurtosis coefficient, and dip angle of MSV fracture surfaces are 1.02 mm, 4.05 and 12.52°, respectively, much larger than those of MSPs and NFPs, which means the MSV samples have the roughest surfaces.
(2) Fracture space reconstruction displays that the NFPs have the biggest initial fracture width (0.362–0.443 mm), then followed by MSPs (0.232–0.237 mm) and MSVs (0.161–0.193 mm), and the inhomogeneous corrosion during long-term geological process may account for the relatively large space of natural fractures.
(3) Fracture surface slippage can increase the fracture width by several times and the critical slipping distance is about 4.0–7.0 mm. Thanks to the mismatch and support of surface asperities, the slipped MSVs have the biggest conductivity increasement, then followed by MSPs and NFPs, which accord well with the previous surface roughness features.
(4) Under high closure stress (30–50 MPa), the widths of the slipped fractures fall to 69.0–127.7 μm, just 8.7%–10.7% of the stress-free fracture width. At dry conditions, the MSVs have obvious stronger stress sensitivity due to the surface micro-structures, while after treating with fracturing fluid, the conductivities of MSPs encounters the steepest drop, about 29.8%–61.7% due to the bedding structures and clay mineral hydrations of shale.
(5) The results can provide reliable parameters for post-fracturing evaluation and productivity forecasting model, so as to accurately assess the contributions of IU fractures to the total shale gas production.

CRediT authorship contribution statement

Bin Yang: Writing – review & editing, Writing – original draft, Methodology, Investigation, Formal analysis. **Wen-Jing Ma:** Writing – original draft, Methodology, Investigation, Formal analysis. **Guan-Chang Pan:** Visualization, Methodology, Formal analysis. **Ke-Liu Wu:** Resources, Methodology, Investigation. **Ying Zhong:** Writing – review & editing, Validation, Formal analysis. **Zhang-Xin Chen:** Writing – review & editing, Validation, Formal analysis.

Declaration of competing interest

The authors declare that they have no known competing financial interests or personal relationships that could have appeared to influence the work reported in this paper.

Acknowledgments

This work was supported by the National Natural Science Youth Foundation of China (No. 52104003), the Open Fund of Engineering Research Center of Development and Management for Low to Ultra-Low Permeability Oil & Gas Reservoirs in West China, Ministry of Education (No. KFJJ-XB-2020-5), the Science and Technology Planning Project of Sichuan Province (No. 22NSFSC4005), the National Natural Science Foundation of China (No. 52274031 and No. 52374005) and the Natural Science Youth Foundation of Sichuan Province (No. 2023NSFSC0930).

References

Ban, L.R., Qi, C.Z., Shan, R.L., Chen, H.X., Jiang, K., Xue, Y.D., 2018. An improved GW model considering the changing curvature radius of asperities. Journal of Mining Science and Technology 3 (5), 442–450. https://doi.org/10.19606/j.cnki.jmst.2018.05.004 (in Chinese).

Briggs, K., Hill, A.D., Zhu, D., Olson, K., 2014. The relationship between rock properties and fracture conductivity in the fayetteville shale. In: SPE Annual Technical Conference and Exhibition. https://doi.org/10.2118/170790-MS.

Bush, A.W., Gibson, R.D., Thomas, T.R., 1975. The elastic contact of a rough surface. Wear 35 (1), 87–111. https://doi.org/10.1016/0043-1648(75)90145-3.

Cai, Z., Yao, F., Tang, Z., 2013. Digital image inpainting with kriging method. J. Computer-Aided Des. Comput. Graph. 25 (9), 1281–1287 (in Chinese).

Chen, P., Han, Q., Ma, T.S., Lin, D., 2015. The mechanical properties of shale based on micro-indentation test. Petrol. Explor. Dev. 42 (5), 723–732. https://doi.org/10.1016/S1876-3804(15)30069-0.

Cipolla, C.L.L., Lolon, E.P.P., Erdle, J.C.C., Rubin, B., 2010. Reservoir modeling in shale-gas reservoirs. SPE Reservoir Eval. Eng. 13 (4), 638–653. https://doi.org/10.2118/125530-PA.

Dam, D.B.V., Pater, C.J.D., Romijn, R., 2000. Analysis of hydraulic fracture closure in laboratory experiments. SPE Prod. Oper. 15 (3), 151–158. https://doi.org/10.2118/65066-PA.

Dieterich, M., Kutchko, B., Goodman, A., 2016. Characterization of marcellus shale and huntersville chert before and after exposure to hydraulic fracturing fluid via feature relocation using field-emission scanning electron microscopy. Fuel 182, 227–235. https://doi.org/10.1016/j.fuel.2016.05.061.

Dong, L.-H., 2018. The Study on Softening Characteristics of Shale Based on Micro-indentation. MS Thesis. China University of Petroleum, Beijing (in Chinese).

Ewy, R.T.T., Stankovic, R.J.J., 2010. Shale swelling, osmosis, and acoustic changes measured under simulated downhole condition. SPE Drill. Complet. 25 (2), 177–186. https://doi.org/10.2118/78160-PA.

Fan, X., Cao, P., Jin, J., 2012. Experimental reasearch on asperity evolution of joint surfaces. Wuhan Ligong Daxue Xuebao/Journal of Wuhan University of Technology 34 (10), 117–121. https://doi.org/10.3963/j.issn.1671-4431.2012.10.024.

Fredd, C.N., McConnell, S.B., Boney, C.L., England, K.W., 2001. Experimental study of fracture conductivity for water-fracturing and conventional fracturing applications. SPE J. 6 (3), 288–298. https://doi.org/10.2118/74138-PA.

Gensterblum, Y., Ghanizadeh, A., Cuss, R.J., Alexandra, A.H., Krooss, B.M., Clarkson, C.R., Harrington, J.F., Zoback, M.D., 2015. Gas transport and storage capacity in shale gas reservoirs – a review. Part A: transport processes. Journal of Unconventional Oil and Gas Resources 12, 87–122. https://doi.org/10.1016/j.juogr.2015.08.001.

Gou, X.H., 2017. Research on Numerical Method for Unpropped Fracture Conductivity of Shale. Ph.D Dissertation. Southwest Petroleum University (in Chinese).

Greenwood, J.A., Tripp, J.H., 1967. The elastic contact of rough spheres. J. Appl. Mech. 34 (1), 153–159. https://doi.org/10.1115/1.3607616.

Guo, T.K., Zhang, S.C., Gao, J., Zhang, J.C., Yu, H.Q., 2013. Experimental study of fracture permeability for stimulated reservoir volume (SRV) in shale formation. Transport Porous Media 98 (3), 525–542. https://doi.org/10.1007/s11242-013-0157-7.

Gutierrez, M., Øino, L.E., Nygård, R., 2000. Stress-dependent permeability of a demineralised fracture in shale. Mar. Petrol. Geol. 17 (8), 895–907. https://doi.org/10.1016/S0264-8172(00)00027-1.

Hanaor, D.A.H., Gan, Y.X., Einav, I., 2015. Contact mechanics of fractal surfaces by spline assisted discretisation. Int. J. Solid Struct. 59, 121–131. https://doi.org/10.1016/j.ijsolstr.2015.01.021.

Jia, S.G., Wan, Y.Y., Wang, Q., Liu, S.D., Liu, Y.M., Wang, Z.C., Ye, Y., Qi, C.Y., 2021. Research on the micro-scale method for testing the mechanical anisotropy of shale. J. Geomechanics 27 (1), 10–18. https://doi.org/10.12090/j.issn.1006-6616.2021.27.01.002 (in Chinese).

Kamali, A., Pournik, M., 2016. Fracture closure and conductivity decline modeling – application in unpropped and acid etched fractures. Journal of Unconventional Oil and Gas Resources 14, 44–55. https://doi.org/10.1016/j.juogr.2016.02.001.

Kang, Y.L., Yang, B., Li, X.C., Yang, J., You, L.J., Chen, Q., 2017. Quantitative characterization of micro forces in shale hydration and field applications. Petrol. Explor. Dev. 44 (2), 328–335. https://doi.org/10.1016/S1876-3804(17)30038-1.

Liu, H.S., Jin, J., Cao, S.F., Ge, S.R., 2011. The quantitative analysis of surface roughness in the dry friction. Chin. J. Mater. Res. 25 (5), 483–488 (in Chinese).

Liu, J., Yao, Y.B., Elsworth, D., 2024. Morphological complexity and azimuthal disorder of evolving pore space in low-maturity oil shale during in-situ thermal upgrading and impacts on permeability. Petrol. Sci. https://doi.org/10.1016/j.petsci.2024.03.020.

Lu, C., Lu, Y., Gou, X.H., Zhong, Y., Chen, C., Guo, J.C., 2020. Influence factors of unpropped fracture conductivity of shale. Energy Sci. Eng. 8 (6), 2024–2043. https://doi.org/10.1002/ese3.645.

Lu, C., Luo, Y., Guo, J.C., Huang, C.H., Ma, L., Luo, B., Zhou, G.Q., Song, M.S., 2022. Numerical investigation of unpropped fracture closure process in shale based on 3D simulation of fracture surface. J. Petrol. Sci. Eng. 208, 109299. https://doi.org/10.1016/j.petrol.2021.109299.

Lu, Z., Jia, Y., Tang, J., Cheng, Y., He, P., Ouyang, L., 2021. Evolution laws of fracture permeability of deep shale in the process of shear slip. Nat. Gas. Ind. 41 (1), 146–153. https://doi.org/10.3787/j.issn.1000-0976.2021.01.013.

Minardi, A., Ferrari, A., Ewy, R., Laloui, L., 2018. The impact of the volumetric swelling behavior on the water uptake of gas shale. J. Nat. Gas Sci. Eng. 49, 132–144. https://doi.org/10.1016/j.jngse.2017.11.001.

Oliver, W.C., Pharr, G.M., 1992. An improved technique for determining hardness and elastic modulus using load and displacement sensing indentation experiments. J. Mater. Res. 7 (6), 1564–1583. https://doi.org/10.1557/JMR.1992.1564.

Pathak, M., Deo, M., Craig, J., Levey, R., 2014. Geologic controls on production of shale play Resources: Case of the Eagle Ford, Bakken and Niobrara. In: SPE/AAPG/SEG Unconventional Resources Technology Conference. https://doi.org/10.15530/URTEC-2014-1922781.

Reece, J.S., Zoback, M.D., Kohli, A.H., 2014. Effect of Shear Slip on Fault Permeability in Shale Reservoir Rocks, H13Q-03. American Geophysical Union. Fall Meeting.

Roussel, N.P., Sharma, M.M., 2011. Optimizing fracture spacing and sequencing in horizontal well fracturing. SPE Prod. Oper. 26 (2), 173–184. https://doi.org/10.2118/127986-PA.

Sakaguchi, K., Tomono, J., Okumura, K., Ogawa, Y., Matsuki, K., 2006. Asperity height and aperture of an artificial tensile fracture of metric size. Rock Mech. Rock Eng. 41, 325–341, 10.1007shu/s00603-005-0102-3.

Sharma, M.M., Manchanda, R., 2015. The Role of induced un-propped (IU) fractures in unconventional oil and gas wells. In: SPE Annual Technical Conference and Exhibition. https://doi.org/10.2118/174946-MS.

Shi, X., Jiang, S., Lu, S.F., He, Z.L., Li, D.J., Wang, Z.X., Xiao, D.S., 2019. Investigation of mechanical properties of bedded shale by nanoindentation tests: a case study on Lower Silurian Longmaxi Formation of Youyang area in southeast Chongqing, China. Petrol. Explor. Dev. 46 (1), 163–172. https://doi.org/10.1016/S1876-3804(19)30016-3.

Wang, L., 2016. The Mechanism of Self-Supporting Fracturing in Daqing's Peripheral Low Permeability Reservoir. Ph.D Dissertation. Northeast Petroleum University (in Chinese).

Warpinski, N.R., Branagan, P.T., Engler, B.P., Wilmer, R., Wolhart, S.L., 1997. Evaluation of a downhole tiltmeter array for monitoring hydraulic fractures. Int. J. Rock Mech. Min. Sci. 34 (3–4), 318.e1–318.e13. https://doi.org/10.1016/S1365-1609(97)00071-3.

Whitehouse, D.J., Archard, J.F., 1970. The properties of random surfaces of significance in their contact. Proc. Math. Phys. Eng. Sci. 316 (1524), 97–121. https://doi.org/10.1098/rspa.1970.0068.

Witherspoon, P.A., Wang, J.S.Y., Wang, K., Iwai, J., Gale, J.E., 1980. Validity of cubic law for fluid flow in a deformable rock fracture. Water Resour. Res. 16 (6), 1016–1024. https://doi.org/10.1029/WR016i006p01016.

Xu, X., 2017. Numerical Simulation Study on Self-Propped Fracture Conductivity in Shale Reservoir. MS Thesis. Southeast Petroleum University (in Chinese).

Zeng, L.B., Liu, W.Y., Xu, X., Tian, H., Lu, S.L., Zhang, M.J., 2022. Development characteristics, formation mechanism and hydrocarbon significance of bedding fractures in typical tight sandstone and shale. Acta Pet. Sin. 43 (2), 180–191 (in Chinese).

Zhang, J., Kamenov, A., Zhu, D., Hill, A.D.D., 2014. Laboratory measurement of hydraulic fracture conductivities in the barnett shale. SPE Prod. Oper. 29 (3), 216–227. https://doi.org/10.2118/163839-PA.

Zhao, H.F., Chen, M., Jin, Y., Ding, Y.H., Wang, Y.H., 2012. Rock fracture kinetics of the facture mesh system in shale gas reservoirs. Petrol. Explor. Dev. 39 (4), 498–503. https://doi.org/10.1016/S1876-3804(12)60067-6.

Zou, S.-Y., Zhang, S.-C., Ma, X.F., 2013. Research on the formation conditions and conductivity of shear fracture for hydraulic fracturing in gas-shale. Sci. Technol. Eng., 138034824 (in Chinese).